Erosive and Strand Burning of Stick Propellants, Part I: Measurements of Burning Rates and Thermal-Wave Structures

W. H. Hsieh,* J. M. Char,† C. Zanotti,‡ and K. K. Kuo§
The Pennsylvania State University, University Park, Pennsylovania 16802

Burning-rate characteristics and thermal-wave structures of NOSOL-363 stick propellant under erosive- and strand-burning conditions were studied using a real-time x-ray radiography system, a strand burner setup, and fine-wire thermocouples. For the erosive-burning rate measurements, locations of instantaneous burning surfaces along the center perforation of a cylindrical propellant grain were determined by comparison of x-ray images obtained during a test and calibration images. The burning rates under strong crossflow conditions, deduced from the instantaneous burning-surface locations, were found to be much higher (up to 2.5 times) than the strand-burning rate of NOSOL-363 stick propellant. This study demonstrated that real-time x-ray radiography is a powerful and reliable tool for nonintrusive measurements of instantaneous burning rates in an optically opaque test chamber. From the strand-burning rate data and thermal-wave structures, a set of important thermochemical properties of NOSOL-363 stick propellant was deduced.

Nomenclature

A_s = preexponential factor, m/s
C_{xy} = normalized cross correlation
$E_{a,s}$ = activation energy, J/mole
$I(\theta)$ = x-ray intensity arriving at the input screen of the image intensifier at an angle of θ, R/s
I_0 = initial x-ray intensity
$L(\theta)$ = interaction length of x-ray and propellant, m
m = linear attenuation coefficient of photoelectric absorption, 1/m
N = total number of pixels
R_u = universal gas constant, J/mole-K
r_b = burning rate, m/s
r_b^0 = strand burning rate, m/s
T_s = burning surface temperature, K
T_o = room temperature, K
$X(n)$ = intensity of x-ray at the nth pixel location of a calibration image, R/s
$Y(n)$ = intensity of x-ray at the nth pixel location of an actual test-firing image, R/s
α_p = thermal diffusivity of a propellant, m^2/s

Introduction

THERE has been increasing interest in the use of single-perforated stick propellants in large-caliber gun systems. In order to accurately analyze and predict the interior ballistic performance of large-caliber gun systems using stick propellants, the erosive- and strand-burning characteristics of the propellants must be determined. Since a typical single-perforated stick propellant [o.d. 6.4 mm (0.252 in.); i.d. 0.86 mm (0.034 in.); length, 686 mm (27 in.)] has a very long perforation, product gases generated from the combustion occurring inside the perforation can pressurize the perforation region. This will cause the product gases to flow from the center toward both ends of the perforation and introduce the erosive-burning effect. Stick-propellant grains recovered from test firings by means of simulated guns[1,2] revealed coning phenomena at both ends of the internal surfaces. This suggests the importance of erosive burning in the combustion of stick propellants.

Erosive burning of various solid propellants was studied extensively under different crossflow situations.[3] However, because of the limitation of existing measurement techniques and hostile experimental conditions, the instantaneous burning-surface locations and erosive-burning rates along the internal perforation of a cylindrical propellant grain could not be determined easily.

In the propellant industry, nonintrusive x-ray radiography techniques[4,5] have been widely used for nonintrusive examination of propellant integrity in rocket motors. They are also used to observe the combustion phenomena of propellants.[6,7] Most previous studies have employed the flash x-ray system. In the present study, a real-time x-ray radiography system[8] is used to determine the instantaneous burning-surface locations along the center perforation of a cylindrical propellant grain.

In the past, no attempt had been made to study thermal-wave structures (subsurface temperature profiles, burning-surface temperatures, dark zone lengths, characteristic times, etc.) of NOSOL-363 stick propellants containing 46% NC, 41% METZRO, 10% TEGDN, and other chemical compounds. Nor had the strand burning rate been measured at low pressures (less than 69 atm). Although the burning-rate exponent for NOSOL-363 stick propellants was found to be 0.965 at high pressures[9] (370–2220 atm), this value may not be suitable for low-pressure conditions; the combustion mechanism of NOSOL-363 stick propellants would vary at different pressure ranges and result in different values of burning-rate exponents.

The objectives of this study are 1) to demonstrate the feasibility of using real-time x-ray radiography to measure the instantaneous burning-surface locations of an axisymmetric stick-propellant grain; 2) to discuss advantages and limitations of the real-time x-ray method for erosive-burning measurements; 3) to use real-time x-ray radiography to measure instantaneous burning-surface locations along the center perforation of NOSOL-363 stick-propellant grains; 4) to determine the strand-burning characteristics of the propellants at pressures lower than 69 atm; 5) to study the thermal-wave structures of NOSOL-363 stick propellants; and 6) to deduce various important thermochemical properties such as burn-

Received July 8, 1988; revision received May 12, 1989.

*Research Associate.

†Graduate Assistant.

‡Visiting Research Associate; currently on leave from Milan CNPM-CNR, Milan, Italy.

§Distinguished Alumni Professor of Mechanical Engineering.

ing-surface temperature as a function of pressure, thermal diffusivity, activation energy and pre-exponential factor for Arrhenius pryolysis law, burning-rate exponent n, and constant a for Saint Robert's burning-rate law.

Method of Approach

Strand-Burning Rate and Thermal-Wave Structure Measurements

A windowed strand burner and fine-wire thermocouples were adopted to measure the strand-burning rate and thermal-wave structure and to characterize the thermophysical properties of the NOSOL-363 stick propellant. Figure 1 shows the schematic diagram of the windowed strand burner. A propellant strand was mounted vertically between two electrical terminal posts. Ignition of the propellant strand was achieved by passing electrical current through a nichrome wire, which was in contact with the top surface of the propellant strand. During the test, a small amount of nitrogen gas flowed continuously from the bottom end to the top end of the chamber. The nitrogen gas flow was used to carry the combustion product gases out of the test chamber so that the windows (on both sides of the test rig) would remain clean for observing combustion phenomena and for recording the instantaneous location of the burning propellant surface.

A scale was optically superimposed on the image of the propellant strand by a semitransparent mirror (Rolyn Dielectric Beam Splitter). A Panasonic VCR was used to record test images and the superimposed scale through the window at the rate of 30 frames/s. The length of the strand burned in a certain amount of time could be precisely measured from the scale superimposed on the test image, and the burning rate could then be determined.

The chamber pressure was measured by a Validyne pressure transducer (DP215) and a carrier demodulator (CD15) with a frequency response of 1000 Hz. The chamber pressure was kept constant by a Skinner solenoid valve (XLB11002), which could be operated at the maximum rate of 10 cps. Operation of the Skinner solenoid valve was controlled by an IBM-AT personal computer. Utilizing the above-mentioned equipment and the accompanying software, pressure fluctuation of the test chamber during a test could be limited to within $\pm 1\%$ of a preselected pressure level (1-69 atm).

In this study, thermal-wave structures of the combustion wave of NOSOL-363 stick propellants under strand-burning conditions are measured by 5-μm and/or 25-μm fine-wire thermocouples. Two different types of thermocouples were used in the tests. Platinum and 13% platinum-rhodium thermocouple wires with diameters of 25 μm were used in tests in which the chamber pressures ranged from 1.7 atm (10 psig) to 28.2 atm (400 psig). For tests in which chamber pressures were higher than 28.2 atm, platinum and 10% platinum-rhodium thermocouple wires with diameters of 5 μm were used.

The detailed description of the experimental setup for producing fine-wire thermocouples and embedding them in the propellant sample is given in Ref. 10. The characteristic time of the solid propellant, thermal diffusivity, and burning-surface temperature of NOSOL-363 stick propellant can be deduced from recorded temperature-time trace by a regression analysis and temperature inflection method.[10-12]

Erosive-Burning Rate Measurement

Experimental Apparatus

An experimental investigation was made to observe the erosive-burning phenomena and to establish a data base for future model validation. Since stick propellants used in large-caliber guns generally have cylindrical geometry with single perforation, it is advantageous to use a test sample with cylindrical geometry to attain close simulation. Under normal circumstances, phenomena occurring in a cylindrical grain cannot be observed by conventional flow-visualization techniques. This is why most researchers in the past have used two-dimensional propellant slabs as test samples. Because a real-time x-ray radiography system is now available for erosive-burning measurements, a test propellant grain with cylindrical geometry can be adopted. In order to allow a relatively

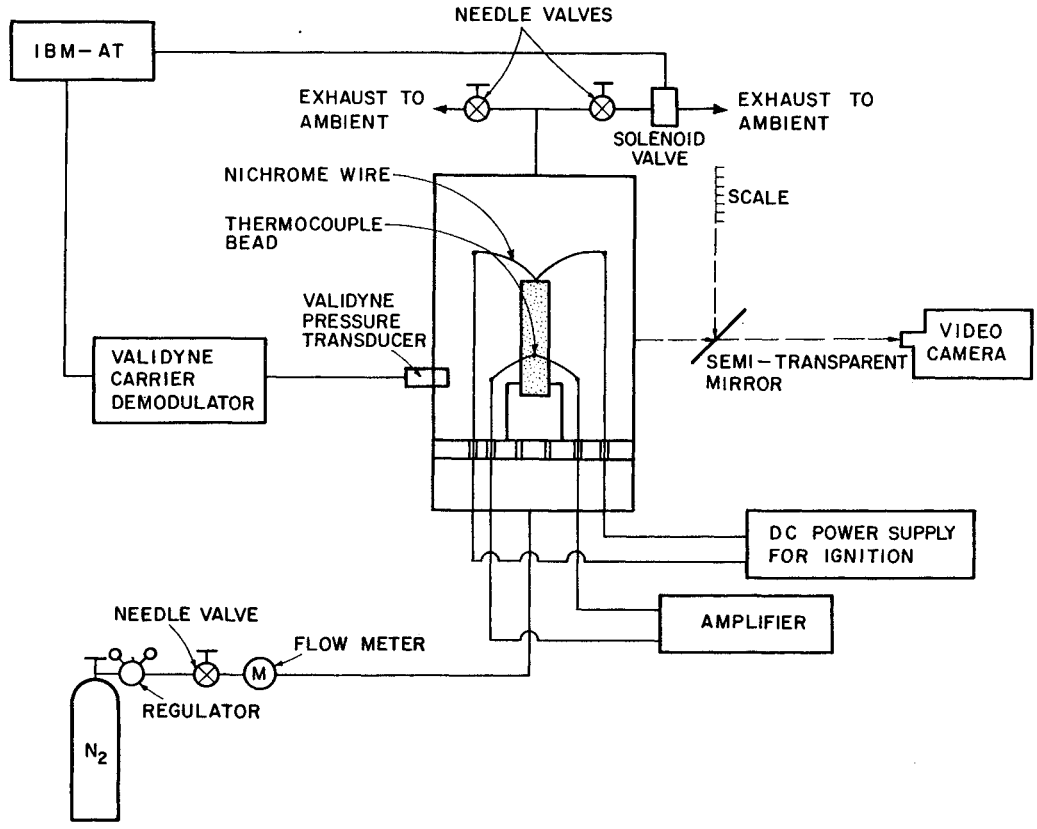

Fig. 1 Schematic diagram of experimental apparatus used in strand-burning tests.

long test duration (a few seconds) for surface regression-rate measurement, a thick-walled cylindrical grain with web thickness in the order of 1 cm has been used. A set of NOSOL-363 propellant samples with 2.54 cm o.d. and 0.48 cm i.d. has been processed for erosive-burning tests.

A test rig was designed and constructed to provide two different configurations, A and B, as shown in Fig. 2. The test chamber of configuration A is made of stainless steel with thermocouple ports for subsurface temperature measurements at various locations. Replacing the exit nozzle with a rupture disc assembly, the propellant grain can be extinguished and recovered by bursting the rupture disc assembly. The main body of the test chamber of configuration B is made of LEXAN materials to facilitate x-ray penetration. Configuration B is also equipped with a fast-actuating ejection mechanism using an explosive bolt to achieve interrupted burning and propellant recovery. In configuration B, the surface regression processes are observed and recorded using real-time x-ray radiography techniques.

Ignition of the propellant charge in the driving motor is accomplished by activating the electric primer via a current input. The combustion products of the propellant charge flow from the driving motor into the test section through a converging graphite nozzle. As hot gases enter the stick-propellant perforation, the test sample is heated quickly to reach a fully ignited condition. The combustion product gases generated from the propellant sample join the product gases from the driving motor and flow through the exit nozzle to the ambient.

Real-Time X-Ray Radiography System

During the test firing with configuration B, the instantaneous burning-surface location of the propellant grain is filmed by a real-time x-ray radiography system.[8] Figure 3 shows the layout of various components in the radiography system. A continuous x ray is generated from the Phillips MG 321 constant potential x-ray system. Two x-ray tubes [one with a focus spot combination of 0.2×0.2 mm/3.0×3.0 mm (MCN 167-160 kV), the other with a focus spot combination of 1.2×1.2 mm/4.0×4.0 mm (MCN 321-320 kV)] are included in the system to satisfy different penetration depth and spatial-resolution requirements.

After passing through the test rig, x-ray signals are transformed to fluorescent light signals on the output screen of a trifield image intensifier (Precise Optics, Model PI 2400 ATF, 4-, 6-, or 9-in. field diameter). The input fluor of the image intensifier is constructed of cesium iodide with a decay-time constant of 650 ns, and the output fluor is a p20 type with a 85-ns decay-time constant. These time constants are short enough to allow the motion analysis system to operate at its maximum framing rate without generating image blur.

The fluorescent light-signal output from the image intensifier is recorded by a Spin Physics 2000 Motion Analysis System or by a Dage camera and Panasonic VCR. The Spin Physics system can record up to 2000 fully digitized frames per second, or up to 12,000 digitized pictures per second with adjustable playback speed.

Digitized data are stored on a high-intensity magnetic recording tape and can be transferred to the Quantex digital image-processing system (QX-9210) frame by frame for analysis through an IEEE-488 interface.

The advantages of using real-time x-ray radiography for erosive-burning measurements are summarized below.

1) No viewing window is needed to record the erosive-burning event since it is possible to observe the surface regression process occurring in a steel or optically opaque chamber with this technique.

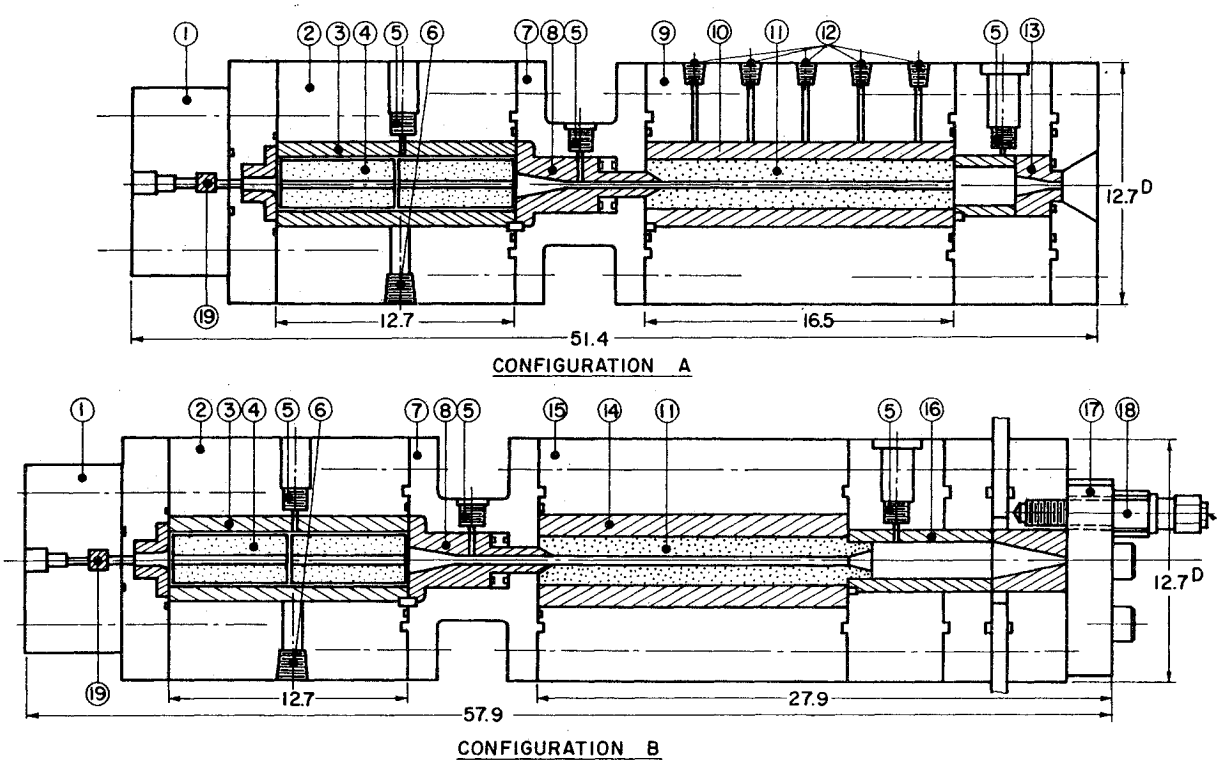

Fig. 2 Schematic diagram of test rig assembly for studying erosive-burning phenomena of stick propellants.

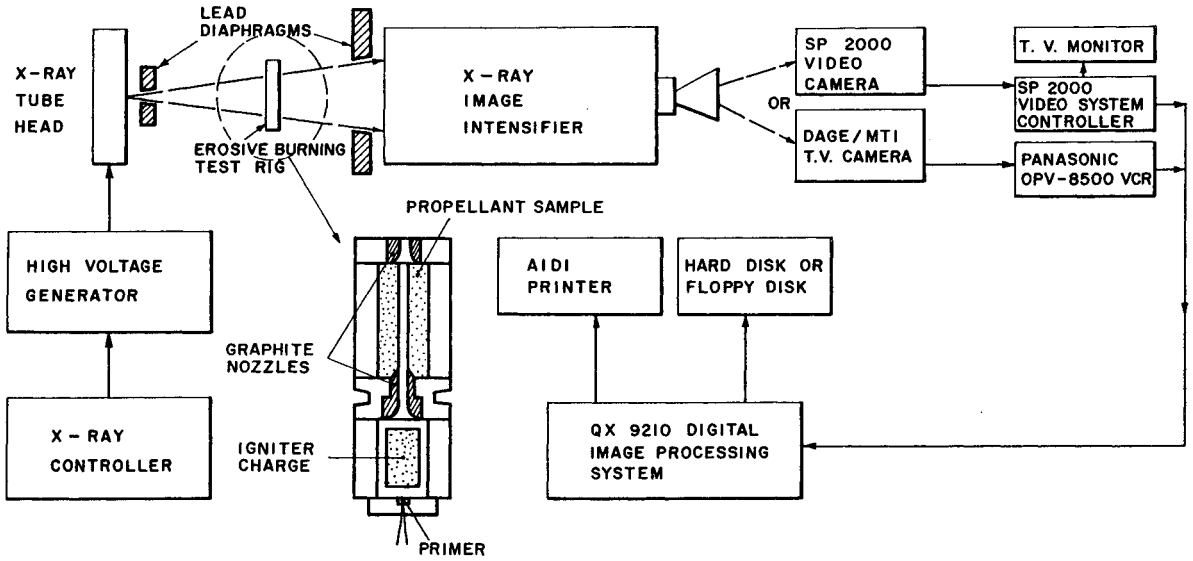

Fig. 3 Layout of real-time x-ray radiograph system.

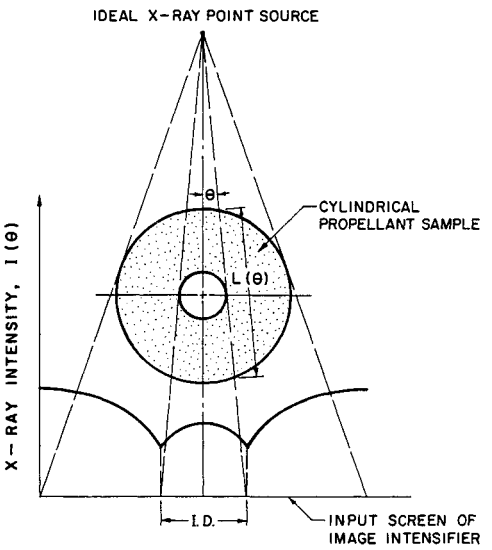

Fig. 4 X-ray intensity distribution of a hollow cylinder under idealized conditions.

2) Real-time x-ray radiography is a nonintrusive technique which will not affect the erosive-burning processes.

3) The technique can be applied to either two-dimensional or axisymmetric propellant-grain geometry.

4) It is a real-time data recording system. Pictures captured in the test event can be played back immediately after the test firing at a lower speed for visualization and analysis.

5) All of the data are in digital form and are convenient for recording, analysis, transfer, and storage.

Data Reduction

Despite the advantages listed above, the data-reduction procedures for deducing the instantaneous internal diameter of a burning propellant sample are not straightforward.

Theoretically speaking, an ideal radiography image of a hollow cylindrical solid propellant with known geometry can be determined from the Beer's law with the assumptions that 1) x-ray radiation is generated from a point source via an infinitely small focal spot, 2) x ray is only attenuated by photoelectric absorption, and 3) distribution of x-ray intensity over the input screen of an image intensifier is uniform. As shown in Fig. 4, the x-ray intensity distribution over the input screen of an image intensifier can be evaluated by the following equation.

$$I(\theta) = I_0 \exp[-mL(\theta)] \tag{1}$$

The distribution of x-ray intensity is continuous, but with two cusps at the tangent points of the internal perforation. Even though the existence of cusps is helpful in determining the inner diameter, the continuity of intensity profile makes it difficult to use direct scaling and standard-edge detection to determine the precise internal diameter of a hollow propellant sample. Two-dimensional slab samples would improve the situation since there are drastic intensity discontinuities at the edges between gas and solid propellant surfaces.

However, the image obtained in a test firing is degraded severely and thus the cusps are not as distinct as those in Fig. 4. The physical mechanisms responsible for this degradation are 1) the finite focal-spot size of the x-ray tube head which generates a grainy or unclear image, 2) Compton scattering[13] of the test chamber and propellant sample, which becomes more pronounced when x-ray radiation energy becomes higher, 3) the nonuniform intensity distribution of x-ray radiation over the input screen of the image intensifier, and 4) the degradation caused by the image intensifier, camera, and recording system.

To deduce accurately the internal diameter of the propellant sample by image restoration technique, the degradation factors mentioned above must be properly treated. To bypass a number of the difficulties involved in image restoration, the following procedures are adopted in determining the instantaneous location of the internal burning surface of the propellant sample.

1) Generation of calibration image: A set of cylindrical propellant samples was machined to specified internal diameters for calibration purposes. The calibration images were produced by placing the machined propellant samples inside the erosive-burning test rig and exposing them to x-ray radiation at the same intensity level as that for test-firing conditions. The setting on the data-acquisition system for calibration is identical to that used in the actual test firing. To reduce the noise level in the calibration signal, numerous calibration images were obtained and averaged for a single specimen.

2) Comparison of images obtained in actual test firing with calibration images: The intensity distribution of the averaged calibration signals was compared with the intensity distribution of test-firing images. A normalized cross correlation

given by

$$C_{xy} = \frac{\sum_N X(n)Y(n)}{\sqrt{\sum_N X^2(n)}\sqrt{\sum_N Y^2(n)}} \quad (2)$$

3) Determination of internal diameter: The instantaneous internal diameter of the test propellant grain at a given location of the test propellant grain is determined from the best correlation with one of the 27 calibration propellant samples. Using this procedure, the accuracy of the diameter measurement is of the order of 0.4 mm.

Discussion of Results

Strand-Burning Results

In the strand-burning tests, three modes of gas-phase combustion were observed. At pressures lower than 7.8 atm (100 psig), no visible flame appeared in the gas phase. In this mode of gas-phase combustion, known as "fizz burning,"[12] it was observed that relatively large-sized particles (~1 mm) came off the burning surface of the propellant sporadically. At pressure between 7.8–21.4 atm (100–300 psig), bright and unsteady yellowish flames were observed. The visible flames were not stationary, but moved around the propellant surface in upward, downward, and sidewise directions. Also, several flamelets were attached to the propellant surface. The attachment zone is relatively small in comparison with the sample burning-surface area. In this study, this mode of combustion is called "unsteady flame." At pressures higher than 21.4 atm (300 psig), the flame is clearly visible and quite steady. This burning with steady luminous flame is called "steady flame mode"; it is also referred to by Kubota et al.[12] as "flame burning."

The observed luminous flame standoff distance from the propellant surface decreases as pressure increases. The phenomenon of reduction in flame standoff distance as pressure increases was first observed by Crawford and Hugget.[14] They measured the distance between the burning surface and the luminous-flame position for pressures between 20 and 30 atm, and found that the distance was inversely proportional to the cube of the pressure. In this study, the flame standoff distance for NOSOL-363 stick propellants changed from 1.5–0.8 mm as pressure increased from 35–48.6 atm.

The measured strand-burning rate vs ambient pressure is plotted in Fig. 5. Each data point represents the average value of 4–13 measured burning rates. As shown in Fig. 5, the maximum error is close to 5%. Guided by the pressure boundary between the steady-flame mode and the unsteady-flame mode of the gas-phase reaction zone structure, the point of the slope break at 2.17 MPa (300 psig) was selected. Consequently, the burning-rate data can be easily distinguished into two regions separated by the above slope break points. The burning-rate exponents and coefficients for the two different regions are marked on these line segments. Such a slope break has been observed for double-base homogeneous propellants,[15] and is essentially the result of the change of the combustion mechanism and the rate of heat feedback to the propellant surface.

Figure 6 shows a typical thermal-wave structure of a NOSOL-363 stick propellant. In this figure, the following characteristic zones are identified.

Zone I is a condensed-phase zone, which includes an inert heating region and a subsurface reaction region. The condensed-phase zone ends at the burning-surface temperature of 320–540 °C at different pressures.

Zone II is defined as the fizz zone, which extends from the burning surface to the region at which the temperature gradient becomes small. The thickness of the zone is in the order of 80–300 μm, depending upon the pressure level.

Zone III is defined as the dark zone, which extends from the end of the fizz zone to the point at which the temperature begins to increase drastically.

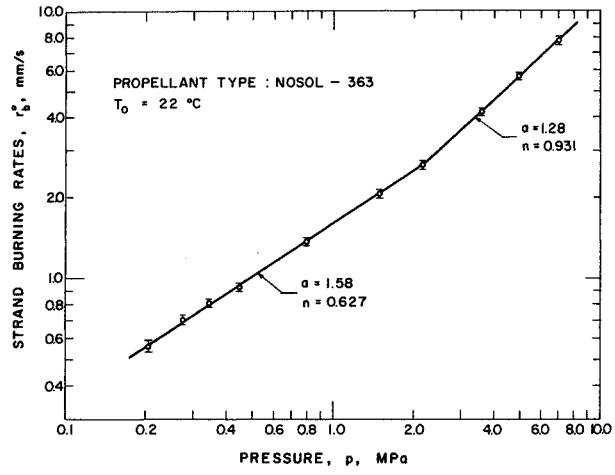

Fig. 5 Strand-burning rates of NOSOL-363 stick propellants at various pressures.

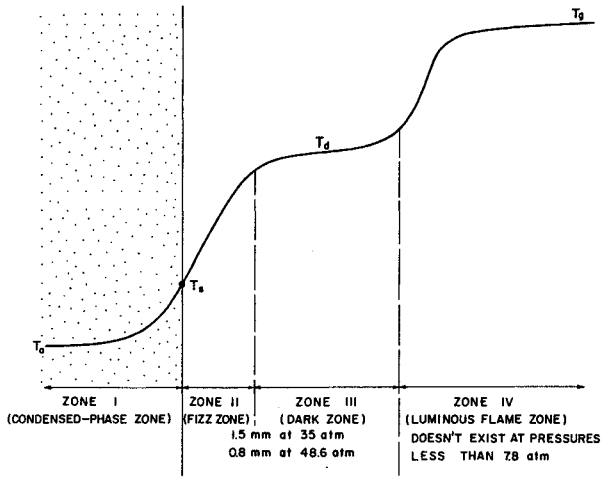

Fig. 6 Schematic description of the flame structure of an NOSOL-363 stick propellant.

Zone IV is the luminous-flame zone, which begins from the point of rapidly increasing temperature.

Thickness of the fizz zone depends on the chemical reaction rate of the gaseous species evolved from the burning surface. The species chemical reaction rate depends on the pressure; the rate increases with increasing pressure. Therefore, the thickness of the fizz zone generally decreases as pressure increases, resulting in an increased temperature gradient and heat feedback from the gas phase to the condensed phase.

In the dark zone (i.e., zone III), the temperature gradient is very small, indicating slow chemical reaction. The peak temperature of the dark zone varies from 1000°C at 3.4 atm (35 psig) to 1200°C at 14.6 atm (200 psig). It increases to 1300°C at 35 atm (500 psig), and to approximately 1500°C at 48.6 atm (700 psig). Further increase in pressure will eventually result in the collapse of the dark zone, but will bring about only a slight increase in maximum temperature in the dark zone.

The pressure dependence of the measured burning-propellant surface temperature is shown in Fig. 7. It is evident that the burning-surface temperature increases with pressure. According to Arrhenius law, the relation between strand-burning rate and burning-surface temperature can be written as

$$r_b^o = A_s \exp[-E_{a,s}/(R_u T_s)] \quad (3)$$

In order to examine the relationship between burning-surface temperatures and strand-burning rates of NOSOL-363 stick propellants, r_b^o vs $1/T_s$ is plotted in Fig. 8. Using least-

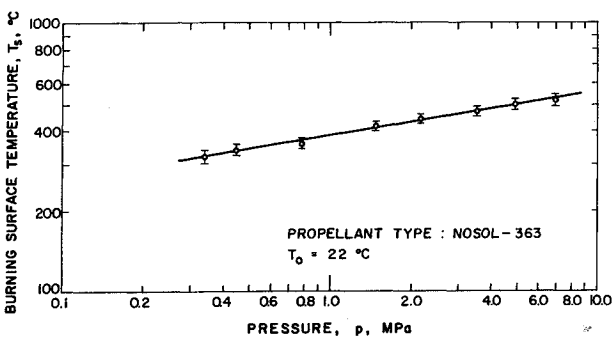

Fig. 7 Variation of burning-surface temperatures as a function of pressure.

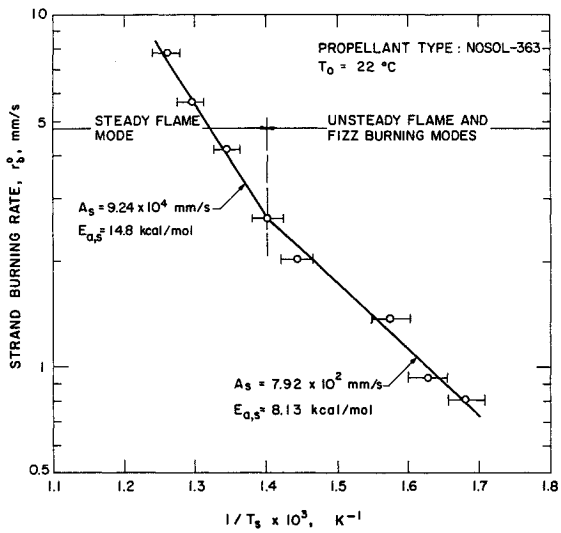

Fig. 8 Relation between strand-burning rates and burning-surface temperatures.

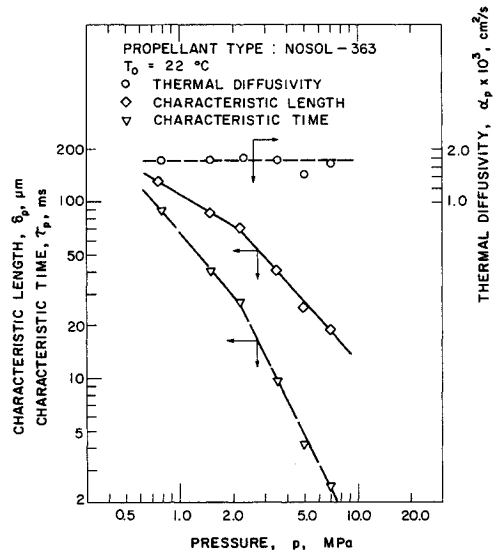

Fig. 9 Variations of thermal diffusivity, characteristic time, and characteristic length of the NOSOL-363 stick propellant as a function of pressure.

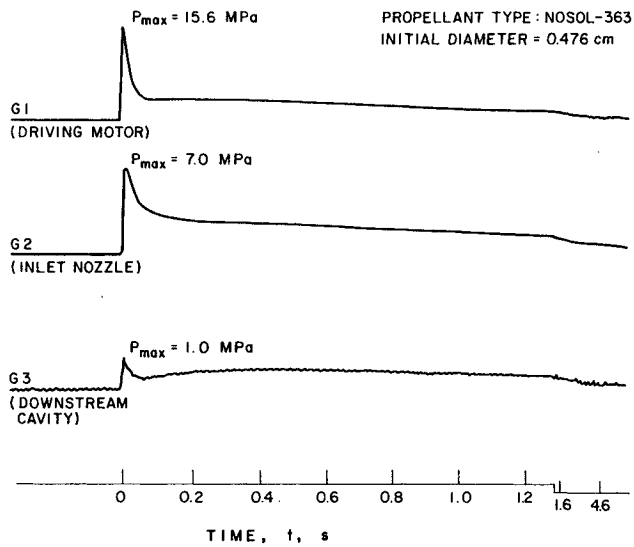

Fig. 10 A typical set of pressure-time traces (test no. ERB-24).

square nonlinear regression analysis, it is found that the $E_{a,s}$ is 8.13 kcal/mole for pressures ranging from 3.4-21.4 atm (35--300 psig) and that the activation energy is 14.8 kcal/mole at pressures between 21.4 and 69.02 atm (300 and 1000 psig).

Several important properties of NOSOL-363 stick propellants can be deduced from the temperature profile in the condensed phase. The thermal diffusivity of the NOSOL-363 propellant (deduced from the condensed-phase temperature profile) is independent of the ambient pressure, as shown in Fig. 9. The characteristic time and characteristic length of NOSOL-363 stick propellants vs pressure are also plotted in Fig. 9. The slope breaks for both curves at 21.4 atm (300 psig) correspond to the change of combustion mechanism from unsteady-flame mode to the steady-flame mode.

Erosive-Burning Results

A typical set of pressure-time traces obtained from the erosive-burning test firing is shown in Fig. 10. All gauges show pressure spikes at initial time. The pressure strike are caused by the strong flow of product gases generated from the driving motor. After the initial spike, the pressures at all gauge locations remain relatively constant, with slight decay.

During the entire test period, the pressure at the driving motor is higher than that at the inlet nozzle or downstream cavity. This implies that the flow is unidirectional from the head end to the exit nozzle. From the magnitude of the pressure at the G3 location, one can be sure that (except at the end of the test firing) the exit nozzle is choked most of the time.

X-ray images of the downstream portion of the test propellant grain were recorded on a videocassette recorder. (Because of the length limitation of the input fluor of the image intensifier, only the downstream portion is recorded.) A typical x-ray image is shown in Fig. 11. It is evident that the inner diameter of the propellant grain can be identified. The increase of internal diameter with respect to time can also be seen on the video screen. After comparison with calibration samples and carrying out data-reduction procedures, the time variations of the inner diameter distributions were determined (see Fig. 12). Using the data presented in Fig. 12, the burning rates at the upstream ($x = x_u = 6.03$ cm) and downstream ($x = x_D = 15.58$ cm) locations were deduced and plotted in Fig. 13.

Some interesting observations made from Figs. 11 and 12 are summarized below.

1) In the early time period ($t < t_3$), the contour of the inner diameter exhibits divergence in the downstream direction due to the strong erosive-burning effect exhibited there. The flow Mach number near the downstream end, x_D, is nearly sonic, and hence has a very high burning rate. The Mach number near the x_u location is also quite high (~ 0.6), but the burning rate is less than that at the x_D location. During this time period, the pressure gradient ($-\partial p/\partial x$) decreases drastically with respect to time, and the perforation area increases

rapidly. Both effects cause the burning rate at x_D to decrease.

2) Between t_3 and t_5, the burning rate at the upstream location catches up to and exceeds that at the x_D location. This is due to the fact that as the perforation area opens, the flow Mach number decreases and the crossflow effect becomes less pronounced. As a result of the higher burning rate at x_u, the contour of the internal perforation becomes uniform.

3) Between t_5 and t_7, the burning rate decreases with respect to time at all locations. During this period, the propellant charge in the driving motor is largely consumed. Because the mass flow rate in the crossflow is produced mainly from the propellant sample, the mass flow rate in the downstream location becomes significantly higher than that in the upstream location. Thus, the rate of decay of the burning rate at x_D is slower than that at x_u. As a result of this variation in burning rate, the contour of the internal perforation again becomes divergent.

4) The diameter distribution of the recovered propellant grain ($t = t_\infty$) between x_u and x_D is shown in Fig. 12. The contour of the port area was quite interesting. The minimum web thickness occurred at $x = 6.05$ cm, and a portion of the grain even exhibited a burn-through. The x-ray image shows a divergent section in the head end of the propellant grain; this is due to the design of the inlet graphite nozzle which protrudes into the propellant grain. Near the end of test firing, as other portions of the propellant surface are extinguished by the low-pressure condition, the weak gaseous jet from the inlet nozzle can still expand and impinge on the inner surface of the propellant grain. Therefore, the burning in this portion during the extinction period produced a convergent-divergent contour.

Another set of data obtained under erosive-burning conditions is shown in Figs. 14 and 15. In Fig. 14, the instantaneous internal diameter of the propellant grain and the total regression rate at an axial station ($x_D = 14.5$ cm) are plotted with respect to time. The instantaneous internal diameter variation was deduced from the real-time x-ray radiography images, and the erosive-burning rate was determined from the differentiation of the polynomial which fits the curve of internal diameter variation. It is quite evident that the burning rate decreases rapidly during the initial time interval, and remains relatively constant after 3 s.

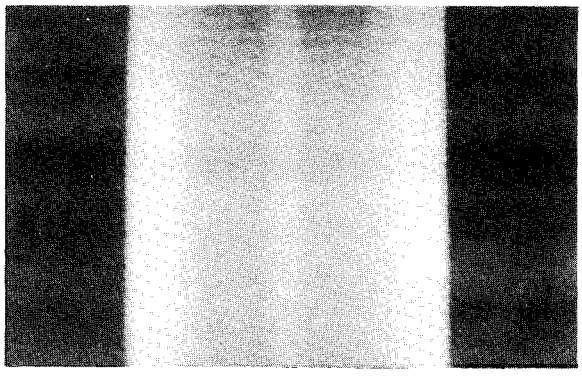

Fig. 11 A typical x-ray image of stick propellant during test firing ERB-24.

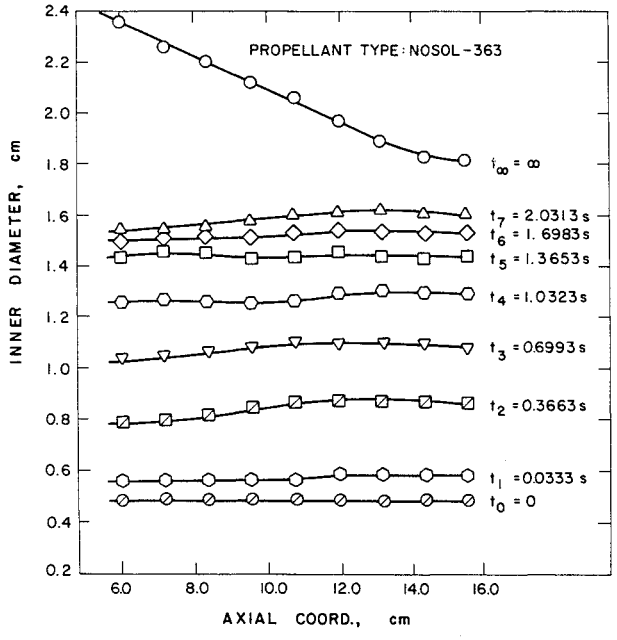

Fig. 12 Time variation of inner diameter distributions deduced from recorded x-ray images.

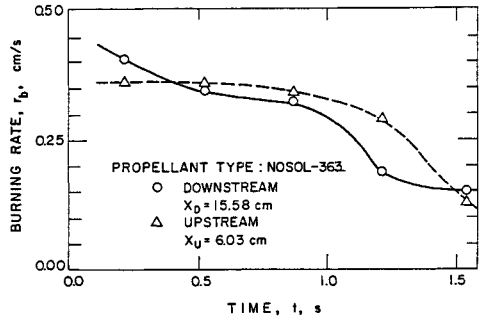

Fig. 13 Measured time variation of erosive-burning rates at upstream and downstream locations.

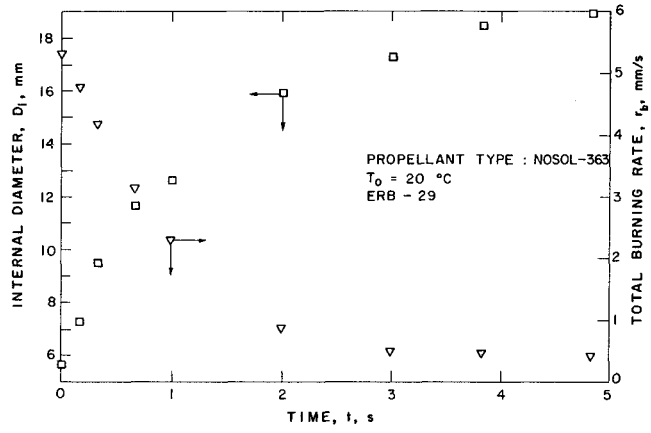

Fig. 14 Time variations of internal diameter and erosive-burning rate obtained from an erosive-burning test (ERB-29).

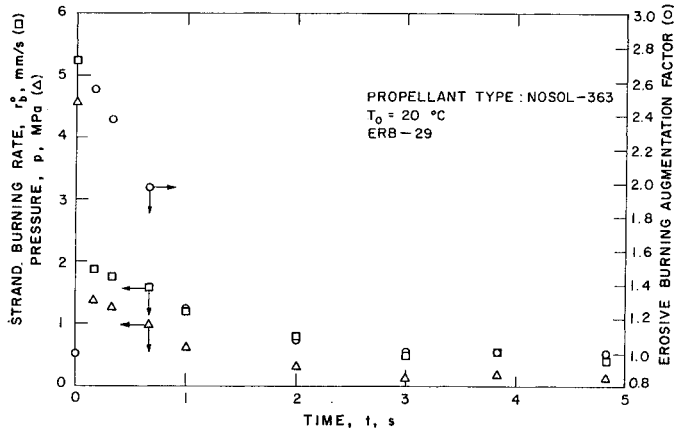

Fig. 15 Time variations of static pressure, strand-burning rate, and erosive-buring augmentation factor obtained from an erosive-burning test (ERB-29).

The pressure-time trace measured at the same axial station is shown in Fig. 15. The strand-burning rate calculated from both the pressure data and burning-rate law and the burning-rate augmentation factor are also plotted in Fig. 15. It is evident that during the initial time interval (less that 2.0 s), the erosive-burning augmentation factor is quite significant. This is in agreement with many observed burning phenomena of center-perforated grains. During the initial time interval, the cross-sectioned area of the flow is small and the mass flow rate per unit area is relatively large; hence, the erosive burning is more pronounced.

Conclusions

Several important conclusions reached in this study are listed below.

1) Real-time x-ray radiography proved to be a nonintrusive, powerful, and reliable tool for determinig erosive-burning rates under confinement conditions.

2) The erosive-burning augmentation factor was found to be very important during the early phase of combustion processes in center-perforated grains.

3) Three modes (fizz, unsteady flame, and steady flame) of gas-phase combustion processes were observed in strand-burning tests of NOSOL-363 propellants.

4) Two different sets of burning-rate exponents and coefficients were deduced from burning-rate data obtained from strand-burner tests. The slope break point at $P = 2.17$ MPa was found to be the boundary of unsteady and steady flame modes.

5) From temperature-time traces obtained in strand-burning tests, burning-surface temperatures were found to be a power law of pressure.

6) The activation energies for NOSOL-363 stick propellants are 8.13 kcal/mole in fizz and unsteady-flame modes, and 14.8 kcal/mole in steady-flame mode. The preexponential factors corresponding to the two flame modes are 79.2 and 9240 cm/s, respectively.

Acknowledgments

This work represents a part of the research results obtained from the project sponsored by the Engineering Sciences Division of the Army Research Office under Contract DAAK29-83-K-0081. The technical program manager is D. M. Mann. His encouragement and support are greatly appreciated. The authors would like to thank F. Robbins of Ballistic Research Laboratory (BRL) for his support and for arranging the processing and shipment of propellant grains required for this investigation. The assistance of K. C. Hsieh of Sverdrup Technology, Inc. in performing some of the erosive-burning tests is also acknowledged.

References

[1]Robbins, F. W., and Horst, A. W., "Continued Study of Stick Propellant Combustion Processes," U.S. Army Ballistic Research Lab., Aberdeen Proving Ground, MD, ARBRL-MR-03296, July 1983.

[2]Hsieh, K. C., and Kuo, K. K., "Numerical Simulation of Combustion Processes of Mobile Stick-Propellant Bundles," 23rd JANNAF Combustion Meeting, Hampton, VA, CPIA Publication 457, Vol. 1, Oct. 1986, pp. 295-306.

[3]Razdan, M. K., and Kuo, K. K., "Fundamentals of Solid-Propellant Combustion," Vol. 90, edited by K.K. Kuo and M. Summerfield, Progress in Astronautics and Aeronautics, AIAA, New York, 1984, Chap. 10.

[4]McIntire, P. (ed.), "Radiography and Radiation Testing," *Nondestructive Testing Handbook,* Vol. 3, 2nd ed., American Society for Nondestructive Testing, Columbus, OH, 1985.

[5]Quinn, R. A., and Sigl, C. C. (eds.), *Radiography in Modern Industry*, Eastman Kodak Co., Rochester, NY, 1980.

[6]Pressley, H., and Glick, R. L., "In-Situ Burning-Rate Determination Using Flash Radiography," 21st JANNAF Combustion Meeting, CPIA Publication 412, Vol. 1, Oct. 1984, pp. 261-274.

[7]Walker, R. Y., Gamble, R. A., and Smith, L. L., "In-Situ Solid Propellant Burn-Rate Measurements Using Flash Cineradiography," Arnold Engineering Development Center, Tullahoma, TN, AEDC-TR-85-22, April 1986.

[8]Kuo, K. K., and Hsieh, W. H., "A High-Speed Nonintrusive Scanning and Recording System," Final Rept. to Office of Naval Research, Contract N00014-84-G-0166, Nov. 1986.

[9]Peters, S. T., "Selected Properties of Navy Gun Propellants," Indian Head Special Publication 84-194, Feb. 1984.

[10]Hsieh, W. H., "Study of Strand and Erosive Burning of NOSOL-363 Stick Propellants," Ph.D. Thesis, The Pennsylvania State Univ., University Park, PA, Aug. 1987.

[11]Liperi, M., "Analisi Sperimentale Mediante Microtermocopple Della Combustione Di Propellanti Solidi Con Proprieta Termiche Variabili," Tesi di Laurea, Dipartmento di Energetica, Politecnico di Milano, 1986.

[12]Kubota, N., Ohlemiller, T. J., Caveny, L. H., and Summerfield, M., "The Mechanism of Super-Rate Burning of Catalyzed Double-Base Propellants," Princeton Univ., Princeton, NJ, AMS Rept. 1087, March 1973.

[13]William, R. H., *Medical Radiation Physics,* Year Book Medical Publishers, Inc. Chicago, Illinois, 1970, pp. 123-142.

[14]Crawford, B. L., Jr., and Hugget, C., "Direct Measurement of Burning Rates by an Electric Timing Method," National Defense Research Committee, Rept. N, A-286, Aug. 1944.